



Charge/Discharge Asymmetry in Blended Lithium-Ion Electrodes

Z. Mao, M. Farkhondeh,* M. Pritzker,** M. Fowler,^z and Z. Chen**

Department of Chemical Engineering, University of Waterloo, Waterloo, Ontario N2L 3G1, Canada

A multi-particle model for blended electrodes has been used to investigate the charge/discharge asymmetry in the response of a $\text{LiNi}_{1/3}\text{Mn}_{1/3}\text{Co}_{1/3}\text{O}_2\text{-LiMn}_2\text{O}_4$ (NMC-LMO) blended cathode at various applied currents. The analysis suggests that the contribution of LMO to the end-capacity of the electrode increases as discharge at higher C-rates progresses but decreases during charge at the same rates. Dynamic analysis of the blended cathode shows that this asymmetric charge/discharge behavior of the blended electrode can be attributed to the difference in the equilibrium potentials of the two components depending on Li concentration and electrode composition and to the differences in the rate of solid-state diffusion of Li and kinetics limitations in LMO and NMC.
© 2016 The Electrochemical Society. [DOI: 10.1149/2.0181702jes] All rights reserved.

Manuscript submitted October 5, 2016; revised manuscript received November 15, 2016. Published December 6, 2016.

As an important energy storage unit, lithium-ion batteries (LIB) have been successfully deployed in high-power portable electronics and communication devices. Furthermore, in order to meet the dramatic growth of the electric vehicle market, well-optimized LIBs will have to satisfy the demanding energy and power density requirements for hybrid-electric (HEV) and plug-in hybrid-electric (PHEV) vehicle applications.¹ Due to their controllable composition and flexible electrode performance, blended cathodes have drawn much attention among researchers.²⁻⁷ These blended cathodes include layered-spinel mixtures ($\text{LiNi}_x\text{Co}_y\text{Al}_{1-x-y}\text{O}_2\text{-LiMn}_2\text{O}_4$ (NCA-LMO),²⁻³ $\text{LiNi}_x\text{Mn}_y\text{Co}_{1-x-y}\text{O}_2\text{-LiMn}_2\text{O}_4$ (NMC-LMO)⁴), layered-layered mixtures ($\text{LiNi}_x\text{Co}_y\text{Al}_{1-x-y}\text{O}_2\text{-LiCoO}_2$ (NCA-LCO)⁵), layered-olivine mixtures ($\text{LiCoO}_2\text{-LiFePO}_4$ (LCO-LFP)⁶), spinel-olivine mixtures ($\text{LiMn}_2\text{O}_4\text{-LiFePO}_4$ (LMO-LFP)⁷). NMC-LMO blended cathodes, among all, have been commercialized by several LIB manufacturers.^{1,4} Layered NMC cathodes have high specific capacity and good capacity retention, while spinel LMO electrodes have a high potential plateau and good rate capability. Hence, the idea behind blending these two components is to combine their best properties and tune the electrochemical performance in terms of energy and power density depending on the proportion in which they are mixed.

The NMC-LMO blended system has been the subject of research by several groups. For example, Smith et al.⁸ and Kitao et al.⁹ found that the cycling and storage degradation of the blended cathode was significantly suppressed compared to that of single-component LMO electrodes due to the interaction between the two active materials. Similar results were also reported by Jeong et al.¹⁰ The aging of NMC-LMO blended cathodes has also been investigated by a number of researchers. Fujimoto et al.¹¹ focused on the changes in structure of the active cathode material particle surfaces after a high-temperature storage. Waldmann et al.¹² conducted post-mortem examinations of commercial 18650-type cells containing a NMC-LMO electrode to characterize aging over low and high temperature ranges of -20°C to 25°C and 25°C to 70°C , respectively. Stevens et al.¹³ carried out high precision coulometry measurements on large-scale NMC-LMO/graphite pouch cells to analyze degradation after storage for 2 years at 30% state-of-charge. Roder et al.¹⁴ studied the impact of calendar aging on the thermal stability of NMC-LMO/graphite cell from the point of assessing safety concerns, while Dubarry et al.¹⁵ evaluated the effect of thermal excursions on lithium-ion batteries to assess the path dependence of their degradation. The entropy coefficient of a blended cathode was determined from open-circuit potential measurements by Huang et al.¹⁶ In addition, a semi-empirical cycle life model was proposed by Cordoba-Arenas et al.¹⁷ to describe the capacity and power fade of a blended cathode battery.

Some researchers who have studied the charge-discharge behavior of blended cathodes have focused on the reversibility of the active material phase change. For example, Nam et al.¹⁸ used in situ

X-ray diffraction to verify that the structural change of the NMC-LMO blended cathode (1:1 wt%) is reversible during charge-discharge at the C-rate of C/2. However, as with most Li-ion battery electrodes, an asymmetry in the electrochemical performance of blended electrodes during charge and discharge is commonly observed. To date, no detailed study of the general evolution of the charge/discharge of a blended electrode system has been reported, let alone any focus on this asymmetry in the charge/discharge response.

Physics-based mathematical models are effective tools to optimize the design of battery electrodes and analyze their electrochemical behavior by simulating the electrode response to an external perturbation. A model provides access to quantities that are sometimes difficult to directly measure experimentally. More specifically, a mathematical model describing the response of a blended electrode can be used to investigate the lithiation/delithiation dynamics of each component during the electrode operation and improve electrode design for specific applications.

Few mathematical models of blended electrode systems can be found in the literature. Albertus et al.² reported a NCA-LMO blended electrode model to describe the distribution of the contact resistance between the component materials. Jung⁴ presented a model of a battery consisting of an NMC-LMO cathode and a graphite-soft anode and examined the effect of the proportion of the two components in the cathode on battery behavior.

As noted above, a detailed analysis of the charge/discharge of a blended electrode system has not previously been reported. Accordingly, in the current study, we carry out a series of galvanostatic charge/discharge experiments on coin cells containing NMC-LMO blended cathodes over a wide range of currents ranging from C/25 to 2C. As will be shown, these experiments reveal an asymmetry between the charge and discharge behavior in the rate capability of this system. In a previous study,¹⁹ we presented a method to accurately predict the composition of a NMC-LMO blended cathode by fitting a single particle model to experimental potential-capacity and different capacity curves at a low C-rate. In a following publication,²⁰ the model was embedded into a pseudo-two-dimensional (P2D) framework to simulate continuous galvanostatic discharges at various operating conditions. The model features multiple particle sizes and different active materials.²⁰ In the current work, a similar multi-particle model is used to examine the asymmetry between the galvanostatic charge and discharge in the NMC-LMO blended cathode operating at the different C-rates. Possible reasons for this asymmetry are analyzed using this multi-particle model.

Experimental

The experimental procedure followed in this work involved dismantling a commercial pouch cell, assembling coin cells and performing galvanostatic charge and discharge experiments. A fresh pouch cell was opened and a piece of the blended NMC-LMO cathode sheet (double-side-coated aluminum current collector) was removed. N-methyl-2-pyrrolidone (NMP) was used to remove one side of the coating layer from the cathode sheet. Circular electrodes with an area

*Electrochemical Society Student Member.

**Electrochemical Society Member.

^zE-mail: mfowler@uwaterloo.ca

Table I. Summary of governing equations and corresponding boundary conditions.²⁰

Particle-level equations	
Solid phase mass balance	Boundary conditions
$\frac{\partial c_{n,m}}{\partial t} = \frac{1}{r^2} \frac{\partial}{\partial r} (D_{n,m} r^2 \frac{\partial c_{n,m}}{\partial r})$ $D_{n,m} = \alpha_{n,m} \mathcal{D}_n$ $\alpha_{n,m} = -\frac{F}{RT} y_{n,m} (1 - y_{n,m}) \frac{\partial U_{n,m}}{\partial y_{n,m}}$ $i_{n,m} = i_{n,m}^0 \left[\exp\left(\frac{(1-\beta_n)F}{RT} \eta_{n,m}\right) - \exp\left(-\frac{\beta_n F}{RT} \eta_{n,m}\right) \right]$ $i_{n,m}^0 = F k_n (c_e)^{(1-\beta_n)} (c_{s,n,m})^{\beta_n} (c_n^{max} - c_{s,n,m})^{\beta_n}$ $\eta_{n,m} = \Phi_1 - \Phi_2 - U_{n,m}(y_{n,m})$ $y_{n,m} = \frac{c_{n,m}}{c_n^{max}}$	$\frac{\partial c_{n,m}}{\partial r} = 0 \text{ at } r = 0$ $\frac{\partial c_{n,m}}{\partial r} = -\frac{i_{n,m}}{F D_{n,m}} \text{ at } r = R_{n,m}$
Electrode-level equations	
Solid phase charge balance	Boundary conditions
$\mathbf{i}_1 = -\sigma_{eff} \nabla \Phi_1$ $\nabla \cdot \mathbf{i}_1 = -\xi \sum_{n=1}^N \sum_{m=1}^M \xi_{n,m} a_{n,m} i_{n,m}$ $\sum_{n=1}^N \sum_{m=1}^M \xi_{n,m} = 1$ $\xi_{n,m} = \frac{\xi'_{n,m} / \rho_n}{\sum_{q=1}^N \sum_{m=1}^M \xi'_{n,m} / \rho_n}$ $a_{n,m} = \frac{R_{n,m}}{3}$ $E = \Phi_1 _{x=L_{sep}+L} - \Phi_f$	$\mathbf{i}_1 = 0 \text{ at } x = L_{sep}$ $\mathbf{i}_1 = I/A \text{ at } x = L_{sep} + L$
Liquid phase charge balance	Boundary conditions
$\nabla \cdot \mathbf{i}_2 = 0$ $\mathbf{i}_2 = -\kappa_{eff,sep} \nabla \Phi_2 + \frac{2\kappa_{eff,sep} RT (1-t_+^0)}{F c_e} \left(1 + \frac{d \ln f_{\pm}}{d \ln c_e}\right) \nabla c_e$ $\kappa_{eff,sep} = \kappa \epsilon_{sep}^y$ $\nabla \cdot (\mathbf{i}_1 + \mathbf{i}_2) = 0$ $\mathbf{i}_2 = -\kappa_{eff,cat} \nabla \Phi_2 + \frac{2\kappa_{eff,cat} RT (1-t_+^0)}{F c_e} \left(1 + \frac{d \ln f_{\pm}}{d \ln c_e}\right) \nabla c_e$ $\kappa_{eff,cat} = \kappa \epsilon_{cat}^y$	$\Phi_2 = 0 \text{ at } x = 0$ $\mathbf{i}_2 _{sep} = \mathbf{i}_2 _{cat} \text{ at } x = L_{sep}$ $\mathbf{i}_2 _{sep} = \mathbf{i}_2 _{cat} \text{ at } x = L_{sep}$ $\mathbf{i}_2 = 0 \text{ at } x = L_{sep} + L$
Electrolyte mass balance	Boundary conditions
$\epsilon_{sep} \frac{\partial c_e}{\partial t} = \nabla \cdot (\epsilon_{sep} D_{eff,sep} \nabla c_e) - \frac{i_2 \nabla t_+^0}{F}$ $D_{eff,sep} = D_e \epsilon_{sep}^{y-1}$ $\epsilon_{cat} \frac{\partial c_e}{\partial t} = \nabla \cdot (\epsilon_{cat} D_{eff,cat} \nabla c_e) - \frac{i_2 \nabla t_+^0}{F} + \frac{(1-t_+^0) \xi \sum_{n=1}^N \sum_{m=1}^M \xi_{n,m} a_{n,m} i_{n,m}}{F}$ $D_{eff,cat} = D_e \epsilon_{cat}^{y-1}$ $D_e = \frac{c_T}{c_0} \left(1 + \frac{d \ln f_{\pm}}{d \ln c_e}\right) \mathcal{D}_e$	$\epsilon_{sep} \frac{\partial c_e}{\partial x} = -\frac{I(1-t_+^0)}{F D_{eff,sep} A} \text{ at } x = 0$ $\frac{\partial c_e}{\partial x} _{sep} = \frac{\partial c_e}{\partial x} _{cat} \text{ at } x = L_{sep}$ $\frac{\partial c_e}{\partial x} _{sep} = \frac{\partial c_e}{\partial x} _{cat} \text{ at } x = L_{sep}$ $\frac{\partial c_e}{\partial x} = 0 \text{ at } x = L_{sep} + L$
Lithium counter electrode kinetics	
$I = -A i_f^0 \left[\exp\left(\frac{(1-\beta_f)F}{RT} (\Phi_f - \Phi_2)\right) - \exp\left(-\frac{\beta_f F}{RT} (\Phi_f - \Phi_2)\right) \right]$	
Equilibrium potential	
$U_{NMC}(y_{NMC}) = 6.51176 - 8y_{NMC} + 7.1086y_{NMC}^2 - 1.55y_{NMC}^3 - 0.459y_{NMC}^6 - 5.00034 \times 10^8 \exp(135.089y_{NMC}^2 - 118.089)$ $U_{LMO}(y_{LMO}) = 0.225 - 0.392y_{LMO} + 2.2 \tanh[-1010(y_{LMO} - 0.994)] + 1.9 \tanh[-21.4(y_{LMO} - 1.04)] + 0.181 \operatorname{sech}[23.4(y_{LMO} - 0.397)]$ $-0.175 \operatorname{sech}[24.2(y_{LMO} - 0.399)] + 0.0164 \operatorname{sech}[13.1(y_{LMO} - 0.567)] + 0.33 \operatorname{sech}[48.1(y_{LMO} - 1)]$	

of 1.103 cm² were punched from the resulting single-sided aluminum current collector and rinsed with dimethyl carbonate (DMC) to remove any electrolyte salt deposit. The washed electrodes were then used as cathodes in cathode/separator/Li coin cells consisting of Li foil reference/counter electrodes, Celgard 2500 membrane as separator and a 1 M solution of LiPF₆ in a 1:1 (weight basis) mixture of ethylene carbonate (EC) and DMC as electrolyte. The entire process from opening the pouch cell to fabricating the coin cells was carried out in an argon-filled glove box (O₂ < 1 ppm, H₂O < 1 ppm).

The assembled coin cells were subjected to a series of galvanostatic experiments using a Neware CT-3008-5 V10 mA-164-U battery cycler (China) at room temperature. In order to condition the coin cells, 5 consecutive formation cycles were carried out prior to the main experiments in the same way as described in our previous work.²⁰ Following these 5 formation cycles, the coin cells were subjected to the continuous galvanostatic charge/discharge experiments, each of which consisted of the following steps: i) charge at a particular rate

until the upper cutoff potential of 4.2 V was reached, ii) 3 h rest period, iii) charge at C/100 until a potential of 4.2 V was reached, iv) 3 h rest period, v) discharge at the same rate as step i) until the lower cutoff potential of 3.0 V was reached, vi) 3 h rest period, vii) discharge at C/100 until a potential of 3.0 V was reached and viii) 3 h rest period. The purpose of applying the small C/100 current in steps iii) and vii) was to ensure that the electrode was fully lithiated/delithiated by the end of discharge/charge. The applied current in steps i) and v) followed the sequence: C/25, C/10, C/5, C/2 1C and 2C. This entire sequence of C-rates was applied to the same cell. It should be noted that a 1C rate corresponds to 2.0 mA applied current.

Mathematical Model

In order to simulate the potential response of the NMC-LMO blended electrode to the current input, we implement a multi-particle mathematical model describing lithiation/delithiation dynamics at the

Table II. List of model parameters for discharge.²⁰

Parameter	Symbol	LMO	NMC
Cathode area (cm ²)	A		1.013 ^m
Electrode thickness (m)	L		5.7×10^{-5m}
Cathode capacity (Ah)	Q		0.002 ^m
Total active-material volume fraction	ξ		0.558 ¹⁹
Radius of type n particle in size class m (m)	$R_{n,m}$	8.7×10^{-7m}	4.65×10^{-6m} (micron group) 4.35×10^{-7m} (submicron group)
Mass fraction of type n particle among total active materials	$\xi'_{n,m}$	0.3 ¹⁹	0.22 ²⁰ (micron group) 0.48 ²⁰ (submicron group)
Rate constant for charge transfer on type n cathode particle (mol/[m ² s(mol m ⁻³) ^{1.5}])	k_n	3×10^{-1120}	3×10^{-1120}
Binary diffusion coefficient of Li in type n particle (m ² s ⁻¹)	D_n	1.0×10^{-1620}	1.1×10^{-1620}
Capacity of type n particle (Ah kg ⁻¹)	q_n	100 ²	151 ²³
Maximum lithium concentration in type n particle (mol m ⁻³)	c_n^{max}	23339 ²	49761 ²³
Density of type n particle (kg m ⁻³)	ρ_n	4220 ¹⁹	4770 ¹⁹
Charge-transfer coefficient for charge transfer on type n cathode particle	β_n	0.5 ²⁰	0.5 ²⁰
Electrode porosity	ε_{cat}		0.35 ²⁰
Initial electrolyte concentration (mol m ⁻³)	c_e		1000 ^m
Separator thickness (m)	L_{sep}		2.5×10^{-5} Celgard
Lithium ions transference number	t_+^0		0.36 ²⁰
Bulk diffusion coefficient in the electrolyte (m ² s ⁻¹)	D_e		5.2×10^{-1024}
Bulk ionic conductivity of the electrolyte (S m ⁻¹)	κ		1.3 ²⁴
Charge-transfer coefficient for charge transfer on Li foil electrode	β_f		0.5 ²⁰
Separator porosity	ε_{sep}		0.55 ^{Celgard}
Bruggeman exponent	γ		1.5 ²⁰
Effective electronic conductivity (S m ⁻¹)	σ_{eff}		10.10 ^m
Exchange current density on Li foil electrode (A m ⁻²)	i_f^0		20 ²⁰
Faraday constant (C mol ⁻¹)	F		96478
Gas constant (J mol ⁻¹ K ⁻¹)	R		8.314
Temperature (K)	T		298

^m: measured

Celgard: Celgard product data sheet

particle and electrode scales, i.e., a P2D model.^{21–22} The model accounts for the two active materials NMC and LMO, the latter of which can be sub-divided into one group of particles that is submicron in size and a second group that is larger than a micron. The application of this model to simulate the response of coin cells during continuous galvanostatic discharge experiments has been successfully verified in our previous studies.^{19,20} Therefore, the governing equations and model parameters are taken from Ref. 19, 20 without any change and are listed in Table I and Table II, respectively. COMSOL Multiphysics 4.4 is used to simultaneously solve all equations at the particle and electrode scales. This model is then run to predict the response of coin cells during galvanostatic charge and compared to data that we have obtained experimentally under identical conditions.

Results and Discussion

Fitting of model to galvanostatic charge experiments.—The multi-particle model and parameters listed in Table II were found previously to accurately describe the behavior of the blended NMC-LMO electrode during galvanostatic discharge.²⁰ It would be useful

to evaluate the accuracy of the model during charge to further analyze the performance of the blended electrode presented later in this paper. Accordingly, its validity has been assessed by computing potential-capacity curves without adjustment of any model parameters and comparing them to the curves obtained from galvanostatic charge experiments. As shown in Figure 1, good agreement is achieved for the two low C-rates of C/25 and C/10. However, more significant deviations are observed in the remaining curves shown in the figure. Furthermore, the discrepancy appears to grow as the C-rate increases. This indicates that the multi-particle model with the parameter values listed in Table II is not sufficiently accurate to simulate charging at all C-rates.

Differential capacity curves are usually used to describe the electrochemical signatures of active materials and to evaluate the contribution of each component in a blended cathode. The simulated differential capacity curves during charging are compared with experimental data in Figure 2. As discussed in our previous work,¹⁹ the peak at ~3.75 V is associated with NMC, while the other two peaks at ~4.00 V and ~4.14 V are attributed to LMO. Despite discrepancies (e.g., peak positions) between the model and experiment especially

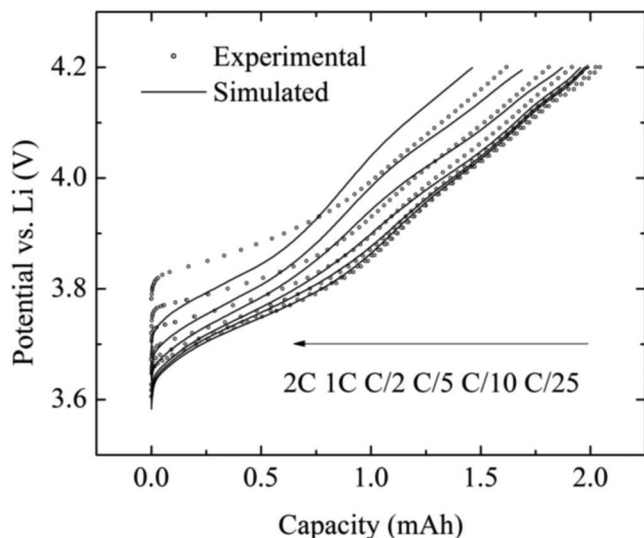


Figure 1. Comparison of the experimental potential-capacity curves during charge of a blended cathode to those computed using the multi-particle model with the parameters in Table II.

at high rates, the characteristic shape of the simulated curves exhibit some similarities with that of the experimental ones. For example, the peak at the highest potential associated with LMO disappears as the charging rate increases, whereas the other LMO peak continues to contribute to the charge capacity.

In order to satisfactorily fit the model to all of the potential-capacity curves over the wide range of applied currents from C/25 to 2C, we adjusted the values of 6 parameters. i.e., the rate constants k_n , solid-state binary diffusion coefficients \mathcal{D}_n and charge-transfer coefficients β_n of LMO and NMC. Note that these parameters are considered to be the same for the sub-micron and micron groups of NMC particles, as was the case in our earlier application of the model to galvanostatic discharge.²⁰ As shown below, the parameters are adjusted to reflect the respective current contribution of each of the various particles within the blended cathode. The parameter values that give the best fit are listed in Table III, while the fitted potential-capacity curves are presented in Figure 3. The match between the simulated and experimental galvanostatic charge curves has now been considerably

Table III. List of model parameters for charge.

Parameter	Symbol	LMO	NMC
Rate constant for charge transfer on type n cathode particle (mol/[m ² s(mol m ⁻³) ^{1.5}])	k_n	3×10^{-12f}	8×10^{-13f}
Binary diffusion coefficient of Li in type n particle (m ² s ⁻¹)	\mathcal{D}_n	2.5×10^{-15f}	5×10^{-15f}
Charge-transfer coefficient for charge transfer on type n cathode particle	β_n	0.45 ^f	0.34 ^f

^fFitted in the current study to the experimental potential-capacity data.

improved. The necessity to adjust the model parameters for the charge simulations may be due to the assumption that the micron-sized NMC particles are non-porous. Comparison of the parameter estimates in Tables II and III shows that the binary diffusion coefficients for the two components obtained from the charge data are about an order-of-magnitude larger than those corresponding to discharge. If the aforementioned assumption regarding the non-porosity of micron-sized NMC particles is valid, an order-of-magnitude increase in the binary diffusion coefficients of the two components implies that solid-state diffusion in the active materials is more strongly controlling during discharge (i.e., high Li concentration) than during charge (i.e., low Li concentration). It should be noted that attempts were made to fit the model to both charge and discharge curves simultaneously using a single set of parameters, but the fits were not satisfactory.

A comparison of the experimental and computed differential capacity-potential curves in Figure 4 also shows an improved match at all charging rates, including the positions of the NMC and LMO peaks. The agreement is particularly good at low C-rates, although less so at higher currents. Note that the computed curves have been obtained using the adjusted parameters given in Table III and correspond to the simulated potential-capacity curves in Figure 3.

Current contribution analysis.—Figures 5a and 5b show the contributions of LMO to the total current (black line) and capacity (blue line) of the blended cathode over the course of charging at C/25 and 2C, calculated according to the simulations before (dash line) and after (solid line) adjusting the six model parameters. LMO begins to delithiate only after about half of the charge time has elapsed and stays active

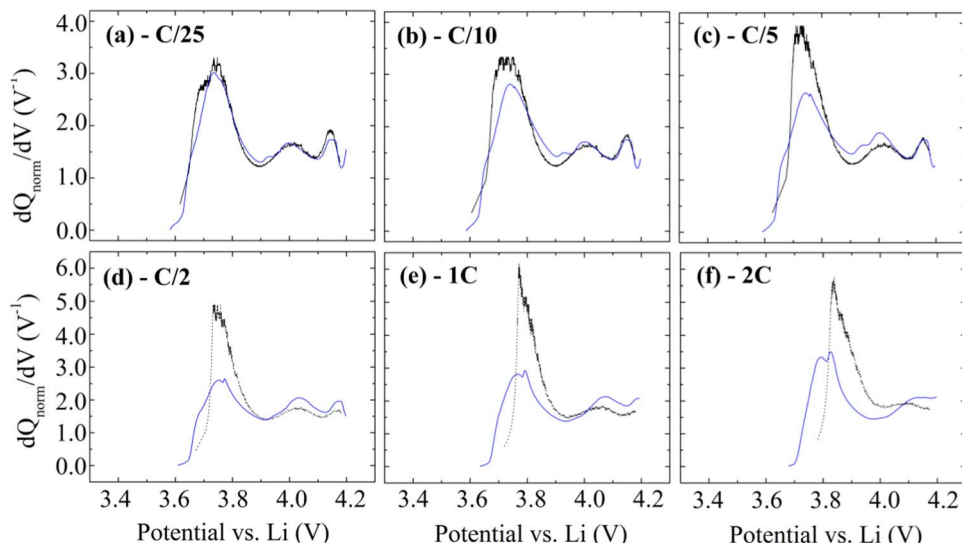


Figure 2. Experimental (black dotted line) and computed (blue solid line) differential capacity curves obtained during charge of NMC-LMO blended electrodes at a C-rate of (a) C/25 (b) C/10 (c) C/5 (d) C/2 (e) 1C and (f) 2C. Model parameters are listed in Table II.

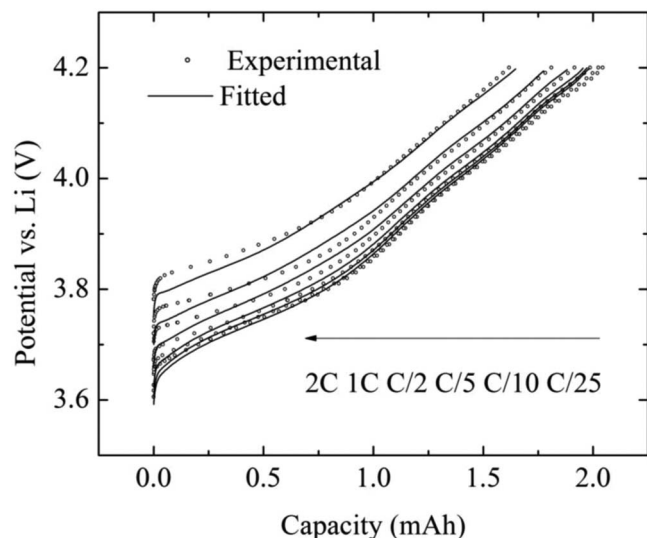


Figure 3. Comparison of the experimental and model-fitted potential-capacity curves using the parameters in Table II and Table III for charge of a blended cathode.

until the end of the charging process. At C/25 (Figure 5a), LMO contributes to the current non-monotonically in three stages: i) negligible during the first stage, ii) sharp increase before leveling off to a plateau at $\sim 50\%$ of total current during the second stage and iii) continued rise by a smaller extent until the electrode is completely delithiated during the third stage. These three stages of delithiation dynamics correspond well to the three differential capacity peaks shown in Figure 4. The NMC peak in the differential capacity-potential curves coincides with the first stage, while the two peaks at higher potentials correspond to the second and third stages.

At a charge rate of 2C (Figure 5b), however, the last delithiation stage vanishes completely in line with the disappearance of the second LMO peak close to the upper cutoff potential. Both simulation sets (solid and dashed lines) follow the same trend at low and high C-rates. They overlap at C/25 but differ more significantly at 2C. The best-fit simulation i.e., after adjusting the model parameters, shows a lower capacity contribution from LMO at 2C compared with that obtained using the original discharge-fitted parameters. Needless to

say, the NMC delithiation complements LMO shown in Figures 5c and 5d. The contribution of NMC to the current and capacity fully dominates the process at both C-rates during the first stage of electrode charging, but then begins to diminish approximately halfway through the process although it remains significant at the end of the process.

Charge/discharge asymmetry.—Figure 6 compares the experimental end-of-charge and end-of-discharge capacities of the blended electrode measured as functions of C-rate. The electrode performs better on charge than on discharge except at 2C. Moreover, the rate capability on charge is more strongly dependent on applied current compared to the discharge rate capability: the achievable charging capacity drops by a larger amount than does the discharge capacity upon increasing the C-rate. Further evidence of this charge/discharge asymmetry is presented in Figure 7 which shows a comparison of the experimental differential capacity curves during charge and discharge. At the low currents of C/25 and C/10, the curves and peak positions for charge and discharge match quite well. The peak positions during both charge and discharge begin to shift when the current is raised to C/5. This is consistent with the previously observed rise in the electrode potential during the charge process and the reduction in the electrode potential during the discharge process when the C-rate is increased.²⁰ An interesting observation from the experimental data shown in Figure 7 is that during discharge the intensity of the peak at ~ 3.75 V (associated with NMC) decreases while that of the peaks at ~ 4.00 V and ~ 4.10 V (associated with LMO) increases as the current is raised from C/25 to 2C.²⁰ The opposite trend is observed during charging, i.e., the former grows, while the latter diminish. Moreover, unlike the discharge process where the two distinct LMO peaks obtained at low rates (C/25, C/10 and C/5) gradually merge into one broad peak at higher rates (C/2, 1C and 2C) are applied, the LMO peak at ~ 4.10 V shifts to higher values and eventually disappears (i.e., it falls beyond the upper cutoff potential) during charge as the C-rate increases.

In summary, the contributions of the blended electrode components differ depending on whether the electrode is being charged or discharged. This trend is observed more clearly when the areas under the differential capacity peaks associated with each component are calculated to determine the contributions of LMO and NMC to the total end-of-charge/discharge capacities at the various applied currents. The computed contribution of each component to the end-of-charge/discharge capacities obtained with both sets of model parameters is plotted as a function of applied current in Figure 8. At the low rate of C/25, the contribution of LMO relative to the total capacity at

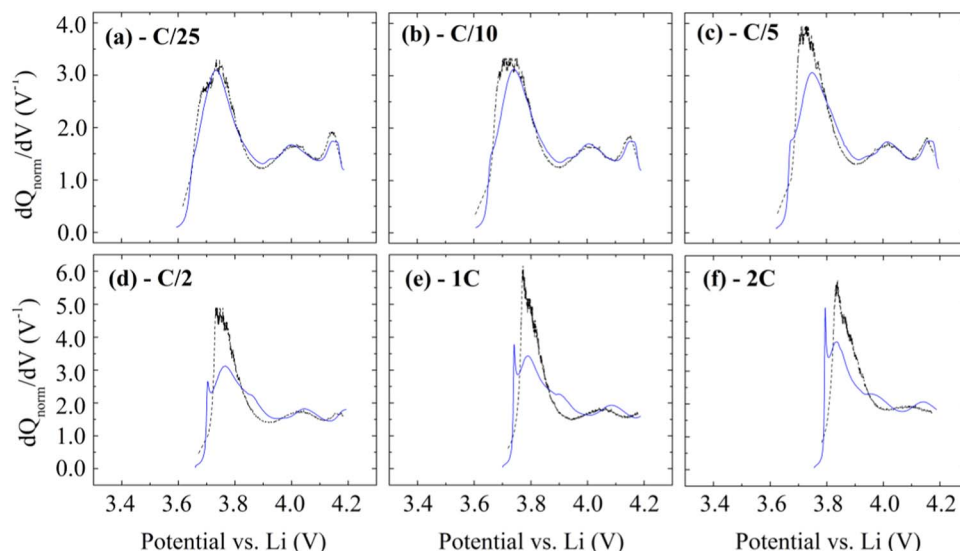


Figure 4. Experimental (black dotted line) and computed (blue solid line) differential capacity-potential curves obtained during charge of NMC-LMO blended electrodes at a C-rate of (a) C/25 (b) C/10 (c) C/5 (d) C/2 (e) 1C and (f) 2C. Model parameters are listed in Table III.

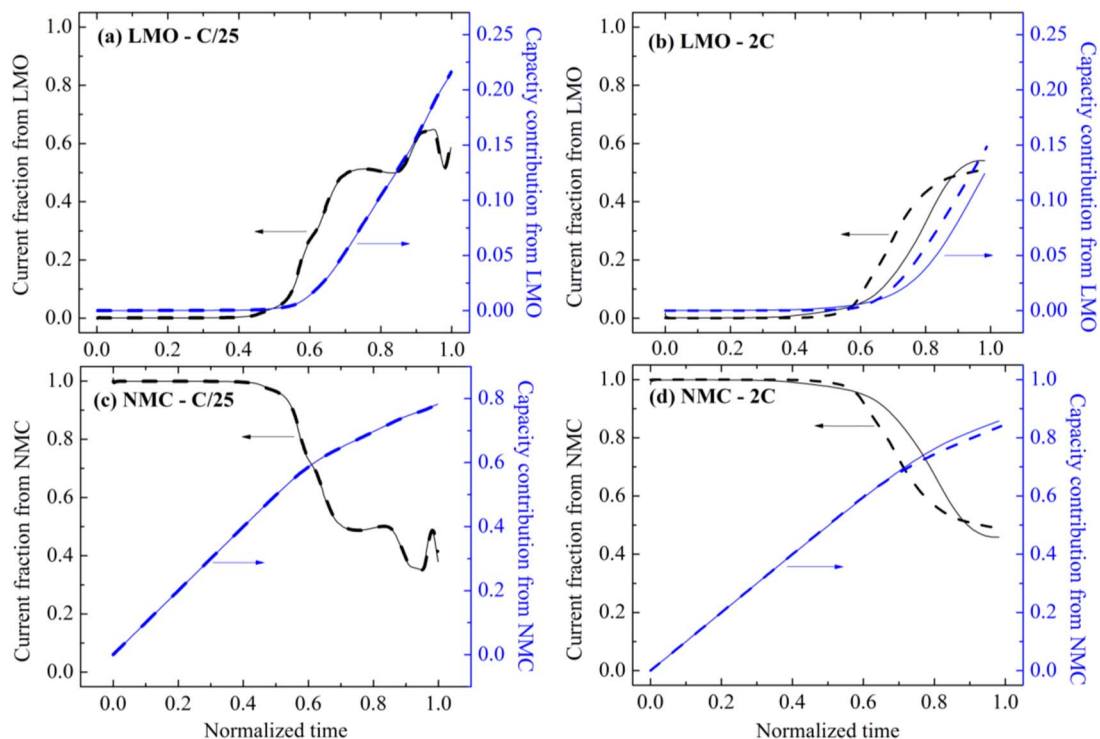


Figure 5. Variation of the current (black line) and capacity (blue line) contributions to the blended cathode charging due to LMO (a, b) and NMC (c, d) with normalized time over the course of a single charge at C/25 (a, c) and 2C (b, d). Calculations are based on simulations before (dashed line) and after (solid line) adjusting the model parameters (Tables II and III, respectively).

the end of charge is very close (~ 0.22) to that at the end of discharge for both sets of charge simulations. The relative contribution of LMO to the electrode capacity during discharge increases if the current is raised, whereas it decreases if the current during charge is raised. Furthermore, the contribution is more strongly dependent on the charge current than on discharge current (Figure 8a) closely resembling the overall charge and discharge rate capability of the electrode shown in Figure 6. The best-fit charge simulations demonstrate an even greater dependence of the component contribution on the charge current. The effect of current on the contribution of LMO is complemented by that acting on NMC which shows the opposite trends (Figure 8b). Altogether, the charge/discharge asymmetry of the blended electrode seen

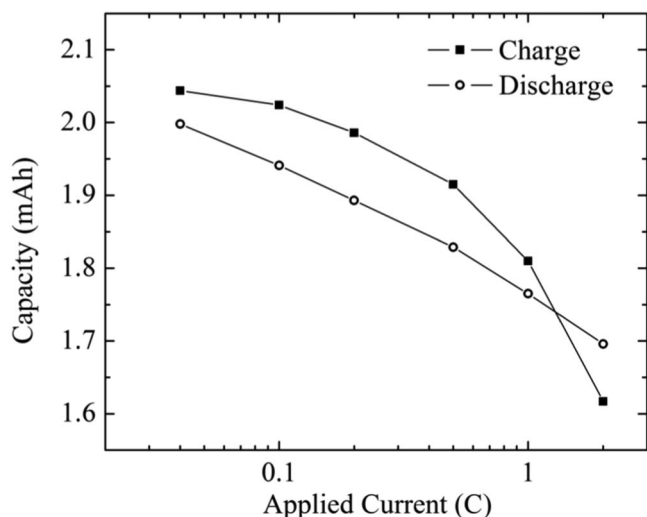


Figure 6. Comparison of the experimental rate capabilities of the NMC-LMO blended electrode during charge and discharge.

in Figure 6 is explained by the asymmetry in the contribution of each component to the electrode capacity and its dependency on current during charge and discharge which is especially pronounced at high C-rates.

The most likely causes of this charge/discharge asymmetry are the: i) difference in the equilibrium potentials of the two active components at any given Li stoichiometry, ii) difference in the “characteristic shape” of the equilibrium potential functions, iii) composition of the blended electrode and iv) differences in the solid-state diffusion and kinetics limitations of the two components. LMO tends to be preferentially lithiated first while NMC is lithiated last during electrode discharge because LMO has a higher equilibrium potential compared to NMC for a wide range of Li stoichiometries (Figure 3 in Ref. 19). Indeed, LMO is almost fully lithiated while NMC is the sole controlling component near the end of a discharge cycle. Figure 9 shows the equilibrium potential curves of pure NMC, pure LMO and the blended electrode as functions of composition approximated by the C/25 discharge curves. Since the discharge rate is so low, the potentials closely approximate the equilibrium potentials of pure NMC, pure LMO and the blended electrode, as discussed in Ref. 19. As shown in Figure 9, at an overall normalized capacity of 0.8, for example, no more LMO can be lithiated during discharge whereas the constant potential tie line at the overall capacity of 0.2 indicates that NMC still has a considerable Li content of ~ 0.12 to be removed during charging. Although the process is dominated by NMC at the beginning of the charge process, it never becomes fully delithiated before LMO does. In contrast to the discharge process, both NMC and LMO are actively involved in the charge process until the upper cutoff potential is reached.

In other words, if the equilibrium potential of NMC and LMO were symmetric with respect to the blended electrode equilibrium potential over the potential range of 3.0–4.2 V, one would expect NMC and LMO particles to undergo the process in the exact opposite order during electrode charge, i.e., complete delithiation of NMC first followed by that of LMO during the remainder of the process. Such symmetry would depend on the characteristic shape of the individual

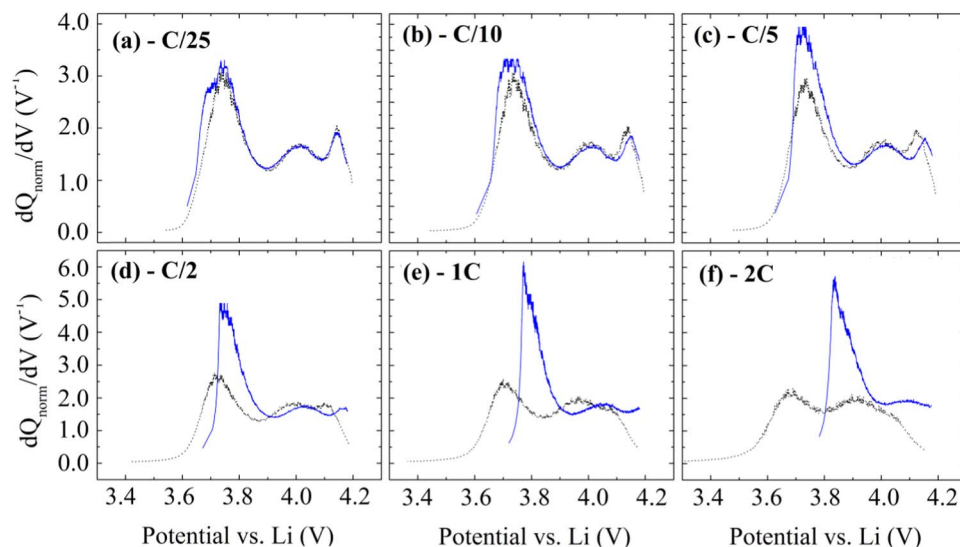


Figure 7. Comparison of experimental differential capacity profiles on charge (blue solid line) and discharge (black dotted line) at rates of (a) C/25 (b) C/10 (c) C/5 (d) C/2 (e) 1C (f) 2C.

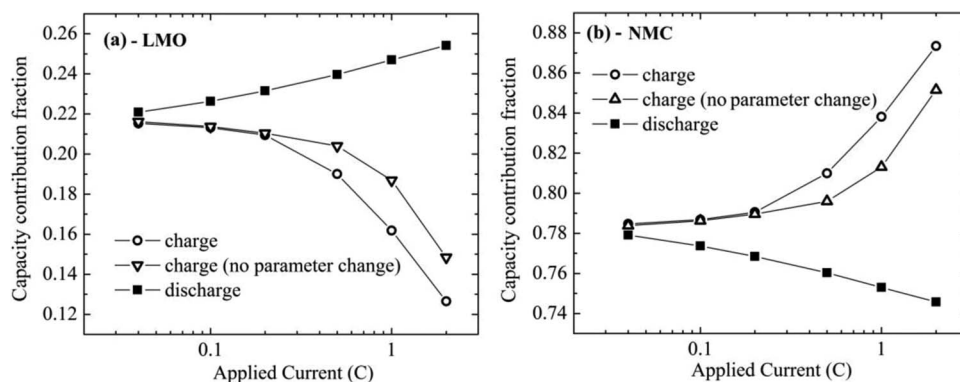


Figure 8. The effect of current on the relative contribution of (a) LMO and (b) NMC to the total end-of-charge/discharge capacities of the blended cathode. The curves are generated using the model before (triangles) and after (circles) adjusting the parameters for charge simulations (Tables II and III, respectively).

equilibrium potential curves and on the composition of the electrode. In the practical case of the blended electrode studied here, a strong dissimilarity between the shapes of the equilibrium potential curves of the two components exists (Figure 9) which leads to different internal dynamics of the electrode during charge than during discharge.

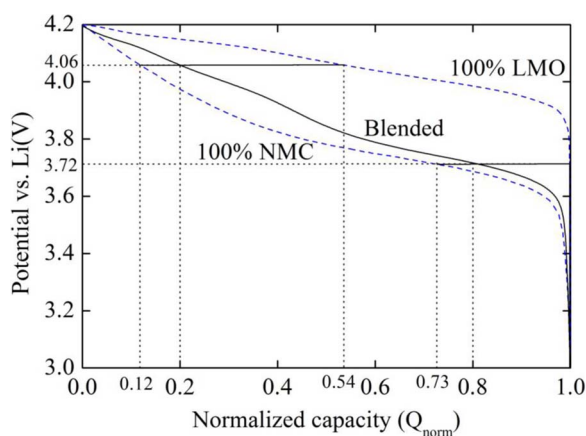


Figure 9. Experimental discharge profile (solid line) of the blended cathode at C/25 and simulated discharge profiles (dashed lines) of pure NMC and LMO cathodes at C/25 (based on Figure 3 in Ref. 19).

In general, diffusion limitations become significant toward the end of a charge and discharge. Thus, whereas Li diffusion in NMC is controlling at the end of discharge, diffusion in both LMO and NMC is limiting at the end of charge according to the above thermodynamic consideration. Therefore, the secondary cause of the charge/discharge asymmetry is dynamic and associated with the differences in the solid-state diffusion within and charge-transfer kinetics at the surface of the two cathode components. As discussed previously, the parameter values that enable the model to closely match the discharge potential-capacity curves fail to do so when the model predictions are compared to the experimental galvanostatic charge data. Moreover, the asymmetric contribution of LMO and NMC to the total capacity at the end charge and discharge, although predicted, is overestimated by the model using the original set of parameter values (Figure 8). The adjustment of the parameters such as the solid-state diffusion coefficients and reaction rate constants (Table III) significantly improves the fit of the model to the experimental charge data including the end-of-charge capacities. This confirms the role that solid-state diffusion and reaction kinetics and their differences between the two components play in the blended electrode charge/discharge asymmetry.

Conclusions

In this work, a multi-particle mathematical model has been used to analyze the charge/discharge asymmetry observed in the rate ca-

pability of an NMC-LMO blended cathode. A comparative study of the differential capacity curves on charge and discharge at different currents levels shows that the asymmetry in the contribution of each component (i.e., LMO or NMC) during charge and discharge at medium to high C-rates is at the heart of electrode charge/discharge asymmetry. It is observed that the capacity contribution of LMO (relative to the total end-of-charge or -discharge capacity at a given rate) increases during discharge when the current is raised, but decreases during charge for a similar change in C-rate.

Based on the model and experiment analysis presented in this paper, the observed asymmetry is attributed to a combination of the following factors:

- i) difference in the equilibrium potentials of the two components as functions of stoichiometry
- ii) composition of the blended electrode
- ii) solid-state diffusion and kinetics limitations which differ for the two components

The first and the second factors together cause an asymmetry in the availability of intercalation sites in the two components toward the end of charge and discharge, while the third factor leads to a difference in the dynamic performance of the electrode during charge and discharge.

Acknowledgment

The authors wish to acknowledge the General Motors Co., Automotive Partnership Canada (Project APCPJ 395996-09) and the Natural Sciences and Engineering Research Council of Canada (Project RGPIN-170912) for financial support.

List of Symbols

A	cathode area (m^2)
$a_{n,m}$	specific surface area of active material n with particle size class m (m^{-1})
$c_{n,m}$	Li ion concentration in active material n with particle size class m (mol m^{-3})
c_e	Li ion concentration in electrolyte (mol m^{-3})
c_T	total Li ion concentration in electrolyte (mol m^{-3})
c_n^{max}	maximum concentration of Li within active material n (mol m^{-3})
D_n	solid-phase binary diffusion coefficient in active material n ($\text{m}^2 \text{s}^{-1}$)
D_e	diffusion coefficient of electrolyte based on a thermodynamic driving force ($\text{m}^2 \text{s}^{-1}$)
$D_{n,m}$	Li ion solid-phase diffusion coefficient in active material n with particle size class m ($\text{m}^2 \text{s}^{-1}$)
$D_{\text{eff,sep}}$	effective diffusion coefficient of electrolyte in separator ($\text{m}^2 \text{s}^{-1}$)
$D_{\text{eff,cat}}$	effective diffusion coefficient of electrolyte in cathode ($\text{m}^2 \text{s}^{-1}$)
D_e	bulk diffusion coefficient in the electrolyte ($\text{m}^2 \text{s}^{-1}$)
E	cell potential (V)
F	Faraday constant (96480 C mol^{-1})
f_{\pm}	mean molar activity coefficient of inorganic salt in electrolyte
I	applied current (A)
$i_{n,m}^0$	exchange current density for lithiation/delithiation on active material n with particle size class m (A m^{-2})
i_1	solid-phase current density (A m^{-2})
i_2	liquid-phase current density (A m^{-2})
$i_{n,m}$	faradaic current density on active material n with particle size class m (A m^{-2})
i_f^0	exchange current density for charge transfer reaction on Li foil (A m^{-2})
k_n	rate constant ($\text{mol m}^{-2} \text{s}^{-1} (\text{mol m}^{-3})^{-3/2}$)
L	electrode thickness (m)
L_{sep}	separator thickness (m)

Q	cathode capacity (Ah)
q_n	practical capacity of type n particle (Ah kg^{-1})
$R_{n,m}$	particle radius of active material n with size class m (m)
R	gas constant ($8.314 \text{ J mol}^{-1} \text{ K}^{-1}$)
r	radial distance within a particle of active material (m)
T	absolute temperature (K)
t	time (s)
t_+^0	lithium ion transference number
$U_{n,m}$	equilibrium potential for lithiation/delithiation on active material n with particle size class m (V)
$y_{n,m}$	lithium content in active material n with particle size class m

Greek

$\alpha_{n,m}$	solid-state thermodynamic factor of active material n with particle size class m
β_n	charge-transfer coefficient for lithiation/delithiation on active material n
β_f	charge-transfer coefficient for charge transfer reaction at lithium foil electrode
γ	Bruggeman exponent
ξ	total volume fraction of all cathode active material in the electrode
$\xi_{n,m}$	volume fraction of active material n with particle size class m
$\xi'_{n,m}$	mass fraction of active material n with particle size class m
ϵ_{cat}	porosity of cathode
ϵ_{sep}	porosity of separator
$\eta_{n,m}$	surface overpotential on active material n with particle size class m (V)
κ	electrolyte ionic conductivity (S m^{-1})
$\kappa_{\text{eff,cat}}$	effective ionic conductivity in blended electrode (S m^{-1})
ρ_n	density of type n particle (kg m^{-3})
σ_{eff}	effective electronic conductivity in blended electrode (S m^{-1})
Φ_1	solid-phase potential of cathode (V)
Φ_2	liquid-phase potential of electrolyte (V)
Φ_f	electrode potential of Li counter electrode (V)

Subscripts

n	active material type (NMC and LMO)
m	particle size class
cat	cathode
eff	effective
sep	separator
s	surface

References

- S. B. Chikkannavar, D. M. Bernardi, and L. Liu, *J. Power Sources*, **248**, 91 (2014).
- P. Albertus, J. Christensen, and J. Newman, *J. Electrochem. Soc.*, **156**, A606 (2009).
- Y. L. Dai, L. Cai, and R. E. White, *J. Power Sources*, **247**, 365 (2014).
- S. Jung, *J. Power Sources*, **264**, 184 (2014).
- J. P. Schmidt, H. Y. Tran, J. Richter, E. Ivers-Tiffée, and M. Wohlfahrt-Mehrens, *J. Power Sources*, **239**, 696 (2013).
- H. S. Kim, M. Kong, K. Kim, I. J. Kim, and H. B. Gu, *J. Electroceramics*, **23**, 219 (2009).
- C. Qiu, L. Liu, F. Du, X. Yang, C. Wang, G. Chen, and Y. Wei, *Chem. Res. Chinese Univ.*, **31**, 270 (2015).
- A. J. Smith, S. R. Smith, T. Byrne, J. C. Burns, and J. R. Dahn, *J. Electrochem. Soc.*, **159**, A1696 (2012).
- H. Kitao, T. Fujihara, K. Takeda, N. Nakanishi, and T. Nohma, *Electrochem. Solid-State Lett.*, **8**, A87 (2005).
- S. K. Jeong, J. S. Shin, K. S. Nahm, T. P. Kumar, and A. M. Stephan, *Mater. Chem. Phys.*, **111**, 213 (2008).
- T. Fujimoto, K. Kitada, K. Yamaura, H. Murayama, K. Ohara, K. Fukuda, and Z. Ogumi. In Meeting Abstracts, *The Electrochemical Society*, **5**, 405 (2015).
- T. Waldmann, M. Wilka, M. Kasper, M. Fleischhammer, and M. Wohlfahrt-Mehrens, *J. Power Sources*, **262**, 129 (2014).

13. D. A. Stevens, R. Y. Ying, R. Fathi, J. N. Reimers, J. E. Harlow, and J. R. Dahn. *J. Electrochem. Soc.*, **161**, A1364 (2014).
14. P. Röder, B. Stiaszny, J. C. Ziegler, N. Baba, P. Lagaly, and H. D. Wiemhöfer. *J. Power Sources*, **268**, 315 (2014).
15. M. Dubarry, C. Truchot, B. Y. Liaw, K. Gering, S. Sazhin, D. Jamison, and C. Michelbacher. *J. Electrochem. Soc.*, **160**, A191 (2013).
16. J. Huang, Z. Li, B. Y. Liaw, Z. Wang, S. Song, N. Wu, and J. Zhang. *J. Electrochem. Soc.*, **162**, A2367 (2015).
17. A. Cordoba-Arenas, S. Onori, Y. Guezennec, and G. Rizzoni. *J. Power Sources*, **278**, 473 (2015).
18. K. W. Nam, W. S. Yoon, H. Shin, K. Y. Chung, S. Choi, and X. Q. Yang. *J. Power Sources*, **192**, 652 (2009).
19. Z. Mao, M. Farkhondeh, M. Pritzker, M. Fowler, Z. Chen, and M. Safari. *J. Electrochem. Soc.*, **162**, A716 (2015).
20. Z. Mao, M. Farkhondeh, M. Pritzker, M. Fowler, and Z. Chen. *J. Electrochem. Soc.*, **163**, A458 (2016).
21. M. Doyle, T. F. Fuller, and J. Newman. *J. Electrochem. Soc.*, **140**, 1526 (1993).
22. J. Newman and K. E. Thomas-Alyea. *Electrochemical Systems*, 3rd ed., Wiley Hoboken, NJ (2004).
23. S. L. Wu, W. Zhang, X. Song, A. K. Shukla, G. Liu, V. Battaglia, and V. Srinivasan. *J. Electrochem. Soc.*, **159**, A438 (2012).
24. M. Farkhondeh, M. Safari, M. Pritzker, M. Fowler, T. Han, J. Wang, and C. Delacourt. *J. Electrochem. Soc.*, **161**, A201 (2014).